Spatial inhomogeneity of point defect properties in refractory multi-principal element alloy with short-range order: A first-principles study

(iD) Tan Shi, Sixin Lyu, (iD) Zhengxiong Su, et al.

COLLECTIONS

Paper published as part of the special topic on Multi-Principal Element Materials: Structure, Property, and Processing

View Online   Export Citation   CrossMark

Spatial inhomogeneity of point defect properties in refractory multi-principal element alloy with short-range order: A first-principles study

Tan Shi,[1] Sixin Lyu,[1] Zhengxiong Su,[1] Yunpeng Wang,[1] Xi Qiu,[2] Dan Sun,[2] Yong Xin,[2] Wenjie Li,[3] Jiang Cao,[4] Qing Peng,[5] Yuanming Li,[2,a)] and Chenyang Lu[1,6,b)]

AFFILIATIONS

[1]School of Nuclear Science and Technology, Xi'an Jiaotong University, Xi'an 710049, China
[2]Nuclear Power Institute of China, Chengdu 610213, China
[3]Science and Technology on Reactor System Design Technology Laboratory, Nuclear Power Institute of China, Chengdu 610213, China
[4]School of Electronic and Optical Engineering, Nanjing University of Science and Technology, Nanjing 210094, China
[5]State Key Laboratory of Nonlinear Mechanics, Institute of Mechanics, Chinese Academy of Sciences, Beijing 100190, China
[6]State Key Laboratory of Multiphase Flow in Power Engineering, Xi'an Jiaotong University, Xi'an 710049, China

Note: This paper is part of the Special Topic on Multi-Principal Element Materials: Structure, Property, and Processing.
[a)]**Electronic mail:** lym_npic@126.com
[b)]**Author to whom correspondence should be addressed:** chenylu@xjtu.edu.cn

ABSTRACT

Short-range order can be developed in multi-principal element alloys and influences the point defect behavior due to the large variation of the local chemical environment. The effect of short-range order on vacancy and interstitial formation energy and migration behavior was studied in body-centered cubic multi-principal element alloy NbZrTi by first-principles calculations. Two short-range order structures created by density functional theory and Monte Carlo method at 500 and 800 K were compared with the structure of random solid solution. Both vacancy and interstitial formation energies increase with the degree of short-range order. Point defect formation energies tend to be higher in regions enriched in Nb and lower in regions enriched in Zr and Ti. Both vacancies and interstitials prefer to migrate toward Zr,Ti-rich regions and away from Nb-rich regions, suggesting that Zr,Ti-rich regions can potentially act as recombination centers for point defect annihilation. Compared to an ideal random solid solution, the short-range order increases the spatial inhomogeneity of point defect energy landscape. Tuning the degree of short-range order by different processing techniques can be a viable strategy to optimize the point defect behavior to achieve enhanced radiation resistance in multi-principal element alloys.

Published under an exclusive license by AIP Publishing. https://doi.org/10.1063/5.0128657

I. INTRODUCTION

Multi-principal element alloys (MPEAs) exhibit excellent mechanical performance,[1,2] good phase stability,[3] and outstanding radiation resistance,[4,5] and are considered promising structural materials for advanced nuclear reactors.[4] The inherent radiation resistance of MPEAs can be largely attributed to the enhanced defect recombination probability and the slower defect evolution induced by the effects of local lattice distortion and sluggish diffusion.[4] In addition, the elemental diversity offers large tunability of

chemical and physical properties for enhanced radiation resistance. The number, species, and concentration of elements can be optimized to obtain the desired alloying effects on defect behavior.[6–8] Besides the compositional tuning, the elemental and microstructural inhomogeneity is also a key factor that influences the radiation defect evolution. The inhomogeneity in MPEAs can have different spatial scales, ranging from atomic-level fluctuation to microstructural fluctuation in form of concentration waves or phase coexistence.[4] Notably, subnanoscale and nanoscale variation of the chemical composition is an important characteristic of

MPEAs. Although MPEAs are usually idealized to be random solid solutions (RSS) due to the high configurational entropy, chemical short-range order (SRO) is inherently present in MPEAs due to the different bonding preferences among constituent species. Recently, direct observation of SRO has been achieved,[9,10] proving its existence in MPEAs. The degree of SRO in the structure can be tuned by applying different annealing temperatures[11–14] or adding small interstitial atoms to change the ordering preference.[15,16] The SRO has been proved to greatly influence the stacking fault energy and dislocation motion,[17,18] showing its significant impact on defect energetics. Therefore, tuning the degree of SRO can be a promising strategy to improve the radiation resistance. However, in order to obtain the desired effect, it is crucial to first understand the role of SRO on defect behavior.[19] In this work, point defects, one of the most basic types of defects, are investigated to reveal the significant impact of SRO on their generation, annihilation, and diffusion, which is relevant for radiation damage studies and diffusion-related properties.

Experimental studies showed that SRO has a profound impact on the irradiation behavior. The nanoscale chemical inhomogeneity was proved to be effective in delaying the radiation defect evolution. It was reported that when NiCoFeCrMn was alloyed with C and N, the SRO was enhanced by the large difference in chemical affinity between principal elements and small interstitial solutes, which contributed to the reduction of void swelling by one order of magnitude compared to NiCoFeCrMn after heavy ion irradiation to a dose level of 50 dpa.[20] It was explained that the roughening of the lattice energy landscape induced by SRO increased the probability of point defect recombination by constraining interstitial diffusion and impeded the movement of defect clusters, which delayed the void formation.[16] In addition to the influence of SRO on radiation defects, the SRO can also evolve during the period of irradiation, suggesting the complex interplay between SRO and irradiation. It was shown that under the condition of heavy ion irradiation at 420 and 540 °C, the fraction of SRO area increased in NiCoFeCrMn, which was attributed to the generation of SRO by the mechanism of radiation-enhanced defect diffusion.[21] In neutron-irradiated NiFeMnCr, measurement of electrical resistivity showed an unusual large increase compared with conventional austenitic Fe–Ni–Cr alloys under similar radiation conditions from four-point probe measurement, suggesting that SRO evolution could occur and contribute to the observed change of resistivity.[22]

In atomistic simulations of defect properties in MPEAs, the RSS structure was usually adopted to study the defect energy, diffusion, and the process of cascade collision.[23–29] The impact of SRO on point defect diffusion has been studied recently by classical potentials for face-centered cubic (FCC) CuNiCoFe, FCC CrCoNi, and BCC MoNbTa.[30,31] These studies showed that SRO could either decrease or enhance the vacancy diffusion and could reduce the interstitial diffusion by localized trapping. The decrease in vacancy diffusion coefficient in CrCoNi was attributed to both the reduced jump rate and enhanced correlated diffusion, whereas the role of diffusion correlation was the dominant reason for reduced vacancy diffusion in MoNbTa.[31] In CuNiCoFe, the chemical ordering effect on vacancy diffusion was found to be significant at low temperature, whereas thermal effect dominated at high temperature.[30] The reduction in interstitial diffusion was mostly attributed

to trapping effect[30] and was expected to promote point defect annihilation and reduce the accumulation of radiation defects.[5] To further utilize the subnanoscale or nanoscale inhomogeneity to enhance radiation resistance, it is important to accurately determine how different degrees of SRO, which can be realized by different processing techniques and conditions, impact both vacancy and interstitial behavior, as their recombination depends on their mutual interactions within an inhomogeneous medium.

Refractory MPEAs with body-centered cubic (BCC) structure are a group of MPEAs with excellent high-temperature performance,[32,33] which is in accordance with the higher operating temperature range that advanced nuclear reactors pursue.[34–36] Refractory MPEAs have also shown great radiation tolerance including reduced void swelling and irradiation hardening.[37,38] However, due to the significant differences in crystal structure and chemical composition compared with FCC MPEAs, the underlying mechanism for radiation resistance is not clearly understood. Currently, a comprehensive evaluation of SRO effects on vacancy and interstitial is still lacking for refractory MPEAs. Due to the severe local lattice distortion and the resulting unique point defect properties of refractory MPEAs,[26,37] a systematic and accurate first-principles study is essential. In this study, the first-principles approach was used to investigate the effects of different degrees of SRO on the defect energy landscape and migration behavior of single vacancy and interstitial in equimolar NbZrTi. NbZrTi was selected as a representative refractory MPEA due to the great mechanical properties and good radiation resistance of NbZrTi and NbZrTi-based high-entropy alloys.[15,32,37,39,40] We showed that different levels of SRO and SRO regions with different elemental enrichment have a large influence on point defect energetics. Both vacancy and interstitial have a tendency to migrate away from the Ni-rich region and toward the Zr,Ti-rich SRO region, leading to spatial dependence of point defect recombination.

II. METHOD

First-principles calculations based on density functional theory (DFT) were performed using the Vienna *ab initio* simulation package (VASP) with the projector augmented wave (PAW) approach and Perdew–Burke–Ernzerhof exchange-correlation functional.[41,42] The studied BCC structure consisted of a $4 \times 4 \times 4$ supercell with 128 atoms ($Nb_{42}Zr_{43}Ti_{43}$). For the Brillouin zone sampling, Monkhorst–Pack k-point meshes of $2 \times 2 \times 2$ and $1 \times 1 \times 1$ were used for static and dynamic simulations, respectively.[43] The convergence criteria for ionic relaxation and electronic self-convergence were 0.01 eV/Å and 10^{-4} eV, respectively. A plane-wave basis cutoff of 400 eV was used. The SRO structures were constructed based on the DFT-based Monte Carlo (MC) approach.[44] In each MC step, swap trials of two random atoms were performed and the total system energy of the new structure was determined. Based on the energy difference with the previous structure, the trial move was adopted with an acceptance probability following the Metropolis–Hastings sampling.[45] Starting from a structure with no SRO, a series of atom swaps were performed until the system energy was stabilized. The system volume was relaxed every 50 steps and only Γ-point was used during the SRO construction. Similar methodology and system size were used to generate

SRO structures in MPEAs with DFT calculations.[44,46] Based on this method, two different degrees of SRO were generated at ~1500–2000 MC steps at a temperature of 500 and 800 K.

For each SRO structure, single vacancy or single interstitial was introduced in the simulation cell at random positions with a total of 90 vacancy configurations and 80 interstitial configurations for the analysis of point defect formation energy. Different initial interstitial configurations were defined including ⟨110⟩ dumbbell, ⟨111⟩ dumbbell, ⟨100⟩ dumbbell, and tetrahedral sites. The vacancy/interstitial formation energy was determined by

$$E_{\text{def}}^{\text{f}} = E_{\text{def}} - E_{\text{per}} \pm \mu_x, \qquad (1)$$

where E_{def} and E_{per} are system energy with and without defect and μ_x is the chemical potential of the removed(+)/added(-) atom.[25] The chemical potential was calculated by the Widom-type substitution method,[47] as described in Ref. 25. For each SRO structure, the atom species were substituted by other species for a total of 20 sets of substitution and it was ensured that the average number of neighbors at the substitution site is close to the stoichiometric ratio. The system energy difference after the substitution corresponds to the energy difference between elemental chemical potentials involved in the substitution. In addition, the total system energy is the sum of the elemental chemical potential multiplied by the number of each element. Based on these relations, the elemental chemical potentials were obtained. The vacancy migration energy was determined by the climbing-image nudged elastic band method with one intermediate image.[48] Three or five intermediate images were also used for cases of irregular energy barrier profiles. More than 120 migration barriers were computed for each SRO structure. For comparison, results of RSS structure were obtained by analyzing the data from Ref. 37 and performing additional simulations. The RSS structure was constructed by the special quasi-random structure (SQS) method.[49] The interstitial diffusion was simulated by *ab initio* molecular dynamics (AIMD) at 1000 K. Five independent runs were performed for each structure for a total of 0.3 ns with a time step of 2 fs using the canonical (NVT) ensemble and Nose–Hoover thermostat. The mean square displacement (MSD) of all atoms and the interstitial defect were calculated according to the method in Refs. 37 and 50. Comparison of vacancy formation energy between k-point meshes of $2 \times 2 \times 2$ and $3 \times 3 \times 3$ was performed for 20 vacancy sites and showed a mean absolute difference of 0.042 eV. The choice of only Γ point for AIMD simulations was also validated by comparing formation energies of vacancies and interstitials of various types with a k-point mesh of $3 \times 3 \times 3$.[37] The charge transfer among atoms was calculated by the Bader charge analysis.[51] The first-principles results were analyzed with the Ovito program and Pymatgen library.[52,53]

III. RESULTS

A. General properties of SRO structures

The SRO structures obtained by the DFT-based MC method at 800 and 500 K are shown in Fig. 1(a) and are hereafter called weak SRO and strong SRO structure for qualitative comparison, as the extent of SRO increases with the decrease in temperature

[see Fig. 1(b)]. As distances between the first nearest neighbor (1NN) and 2NN atom pairs are close and can even overlap in BCC MPEAs, a modified Warren–Cowley SRO parameter is adopted here to account for SRO trends in both 1NN and 2NN and is defined as[46]

$$\alpha_{12}^{ij} = (8\alpha_1^{ij} + 6\alpha_2^{ij})/14, \qquad (2)$$

where α_k^{ij} is the Warren–Cowley SRO parameter of finding atom type j around atom i in the kth neighboring shell.[44,56] We note that the ordering between different element pairs is short-ranged in both structures, as reflected by the small SRO parameters beyond 3NN. Compared with the RSS structure, the energy changes per atom for the weak and strong SRO structure are −9.3 and −19.9 meV/atom, respectively. There is a tendency of segregation between Nb–Zr and Nb–Ti neighbors, corresponding to positive Warren–Cowley SRO parameters shown in Fig. 1(b). This can be qualitatively explained by the higher enthalpy of mixing of Nb–Zr and Nb–Ti pairs relative to Zr–Ti.[57] Correspondingly, there is a clustering tendency of other element pairs including Nb–Nb, Zr–Zr, Zr–Ti, and Ti–Ti pairs. For defect analysis, each structure is classified into Nb-rich, neutral, and Zr,Ti-rich regions where the numbers of Nb in the 1NN and 2NN are ⩾7, between 3 and 7, and ⩽3, respectively. This classification is motivated by the clustering of Nb–Nb and Zr/Ti–Zr/Ti neighbors in the SRO structures. Although the defect properties depend on the specific local environment, the classification into three SRO regions allows statistically significant conclusions to be drawn.

First, structural and atomic properties are examined for the SRO structures. Figure 1(c) shows that with an increased degree of SRO, the deviation of Nb atoms from ideal lattice sites remains almost unchanged. In contrast, the atomic displacements of Zr and Ti atoms have a noticeable increase, especially for Ti atoms. Analysis of the phonon dispersion spectra indicates that both the weak and strong SRO structures are dynamically stable with reduced imaginary component compared to the RSS structure,[58,59] which is also consistent with the observation from HfNbZrTi[60] (see Sec. I of supplementary material for the phonon dispersion analysis). Thus, larger atomic displacement of Zr and Ti atoms can help stabilize the SRO structure. According to the Bader charge analysis, the charge transfer is reduced for all types of atoms due to the clustering of similar types of atoms [see Fig. 1(d)]. Here, we show that local chemical ordering impacts the atomic charge and the resulting atomic stress, which could further influence the defect behavior.[54,61]

B. Vacancy properties

The distributions of vacancy formation energy (E_{f}^{v}) for structures of different degrees of SRO are shown in Fig. 2(a). The wide energy distribution is intrinsic to BCC MPEAs due to the variation of chemical environment and the severe local lattice distortion.[26,28] It can be seen that E_{f}^{v} increases with the degree of SRO with the overall energy distribution shifting to higher energies. The average E_{f}^{v} increases from 1.04 ± 0.45 eV in the RSS structure to 1.54 ± 0.49 eV in the strong SRO structure. For each type of vacancy, the increasing trend with the degree of SRO is also observed [see Fig. 2(b)]. The most significant increase occurs in Nb
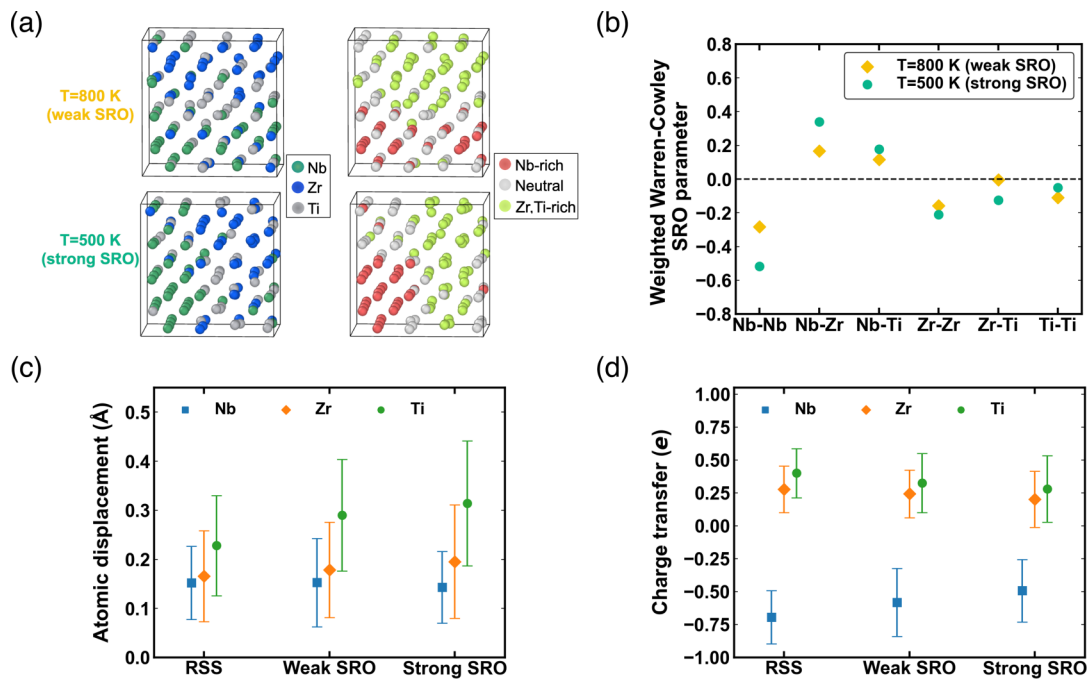
FIG. 1. (a) NbZrTi SRO structures obtained from the Monte Carlo + DFT method at a temperature of 800 and 500 K. The structures are classified into Nb-rich, neutral, and Zr,Ti-rich regions based on the clustering tendency in the 1NN and 2NN. (b) Weighted Warren–Cowley SRO parameter for different SRO structures. (c) Average atom displacement relative to the perfect lattice site and (d) charge transfer for the random solid solution, weak SRO, and strong SRO structure. Positive charge transfer indicates electrons being transferred away.[54] Since the local lattice distortion and charge transfer depend on the specific atomic arrangement,[55] the results in (c) and (d) are averaged over three structures of similar extents of SRO.

vacancy, changing from 0.98 ± 0.45 eV to 1.71 ± 0.50 eV. In the SRO structures, the E_f^v of Nb vacancy tends to be higher and the E_f^v of Ti vacancy tends to be lower. The average relaxed distances per atom after creating a vacancy are 0.122, 0.106, and 0.087 Å for RSS, weak SRO, and strong SRO structures, respectively, indicating less structural adjustment in SRO structures. The fact that RSS is energetically less stable than SRO structures triggers a higher extent of structural relaxation in RSS to reduce the energy of vacancy structure, resulting in a smaller E_f^v. It was reported that vacancy structures in RSS NbZrTi experience instability, i.e., vacancy-atom exchange during structural optimization.[37] The percentages of unstable vacancy configurations are 23%, 16%, and 10% for RSS, weak SRO, and strong SRO, respectively, showing a progressive reduction in the fraction of unstable sites. This also reflects the higher stability of SRO structures. We note that the arithmetic mean and standard deviation presented here are used to show the overall evolution of formation energy among different structures. At thermal equilibrium, the point defect probability density function $\rho(E)$ at a certain formation energy E can be estimated by[62]

$$\rho(E)dE = \frac{\exp(-E/k_b T)f(E)dE}{\int_E \exp(-E/k_b T)f(E)dE}, \tag{3}$$

where $f(E)$ is the probability density function of point defect formation energy of all the possible sites. Although low-energy sites

have lower $f(E)$ near the lower end of the distribution, the $\exp(-E/k_b T)$ term contributes to their higher occurrence probability. Based on Fig. 2(a), the increasing trend of E_f^v from RSS to strong SRO structure still holds at thermal equilibrium, but the energy distribution shifts to lower values. For the non-equilibrium process of generation of radiation defects during the thermal spike period, the energy cost can be considered to be approximately proportional to the average formation energy, as a large number of defects are created in a local region by displacement cascade. However, defects with low formation energy are also favored after the quenching of the cascade.

The E_f^v differs in different SRO regions, as shown in Fig. 2(c). The E_f^v tends to be higher in Nb-rich regions and lower in Zr, Ti-rich regions for both weak and strong SRO structures. In the RSS structure, due to the lower probability of strong elemental clustering, this difference is less noticeable. The different E_f^v in different SRO regions can be reflected by the correlation between E_f^v and the number of each element in the local environment. The dependence of E_f^v of Nb vacancy on the number of each element in 1NN and 2NN is shown in Fig. 3. The results on Zr and Ti vacancy are provided in Sec. II of supplementary material. First, the large statistical variation at a fixed number of neighboring element indicates that E_f^v is also affected by other types of neighboring elements and the relative positions of all the neighbors. This is commonly seen in MPEAs due to chemical disorder and local lattice distortion.[26,27]
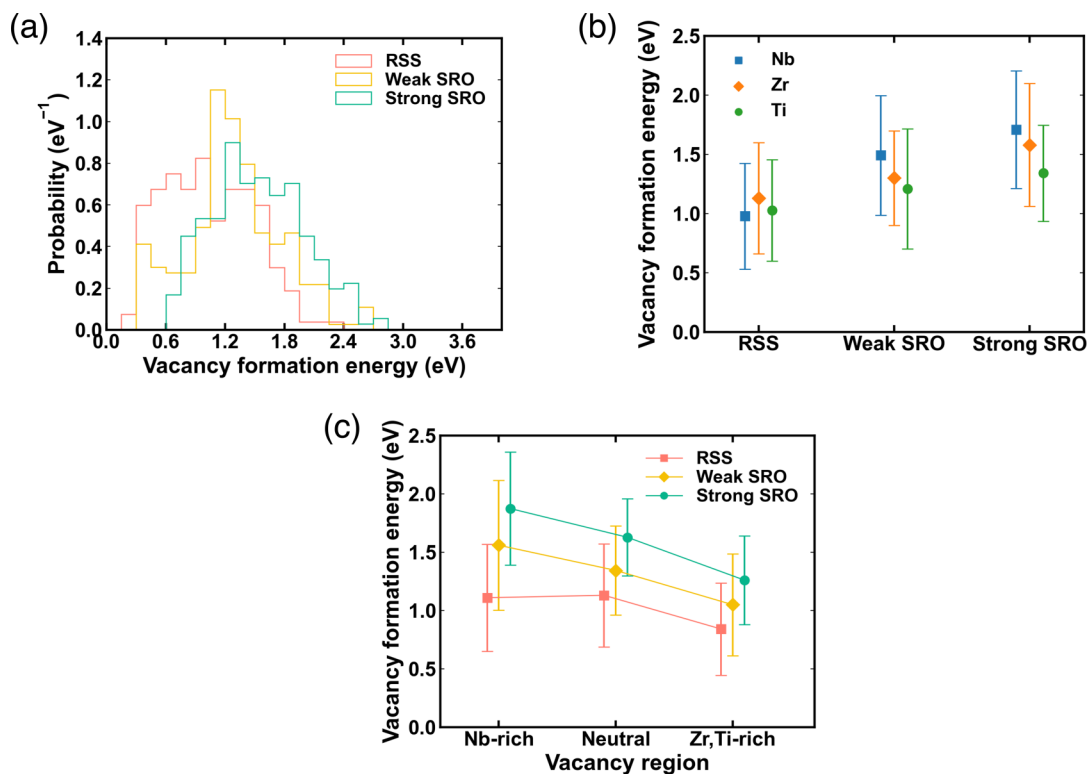
FIG. 2. (a) Distribution of vacancy formation energy for structures of different degrees of SRO. (b) Vacancy formation energy for different types of vacancies. (c) Vacancy formation energy in different SRO regions. The average and standard deviation are used here to represent the statistical variation of formation energy induced by chemical disorder and local lattice distortion.

However, it can be seen that in SRO structures, there is a tendency of increasing E_f^v with the number of Nb neighbors. Extreme E_f^v values occur mostly when Nb is heavily depleted (0 or 1 atom) or heavily enriched ($\geqslant 10$ atoms out of the 14 neighbor atoms), leading to a more obvious change of E_f^v in SRO structures. In contrast, the change of E_f^v with the neighboring elements is insignificant in the RSS structure due to the lower extent of Nb clustering around these vacancy sites. We also note that Fig. 3 does not reflect the spatial distribution of these vacancy sites. The spatial clustering of Nb-rich or Zr,Ti-rich regions in SRO structures have the effect of grouping sites of similar energies, resulting in a more pronounced energy difference among different local SRO regions.

Regarding the vacancy migration energy, all the studied structures exhibit a wide energy distribution ranging from ∼0 to 1.4–1.8 eV [see Fig. 4(a)]. The strong SRO structure has a slightly lower fraction of high-energy barriers. A wide migration energy distribution leads to the preferential migration through low transition barriers. The Pearson correlation between forward and backward migration energy changes from positive to negative from RSS to SRO structures, indicating a different correlation behavior between consecutive vacancy jumps [see Fig. 4(b)]. A positive correlation indicates that the backward migration energy has a similar magnitude as the forward migration energy, whereas a negative

correlation corresponds to a higher proportion of sites with a large difference between the forward and backward migration barrier. Further analysis of vacancy migration direction shows that the vacancy migration from Nb-rich and neutral regions to Zr,Ti-rich regions is facilitated, whereas the migration from Zr,Ti-rich and neutral regions to Nb-rich regions is energetically unfavorable [see Figs. 4(c) and 4(d)]. This is generally true for both SRO structures with a certain statistical fluctuation induced by local chemical complexity. The vacancy migration tendency from the Nb-rich region to neutral region and then to the Zr,Ti-rich region is in accord with the relative order of E_f^v presented in Fig. 2(c), as the difference between forward and backward barrier is caused by the difference between initial and final energy states. The results demonstrate that vacancy migration in SRO NbZrTi exhibits a certain directionality with a tendency to migrate toward Zr,Ti-rich regions.

C. Interstitial properties

Single self-interstitial defect was randomly placed in the SRO structures to study the formation energy variation of self-interstitial in different SRO regions. The distributions of interstitial formation energy (E_f^i) for different SRO structures are shown in Fig. 5(a). The distribution shifts towards higher energies with the increase in
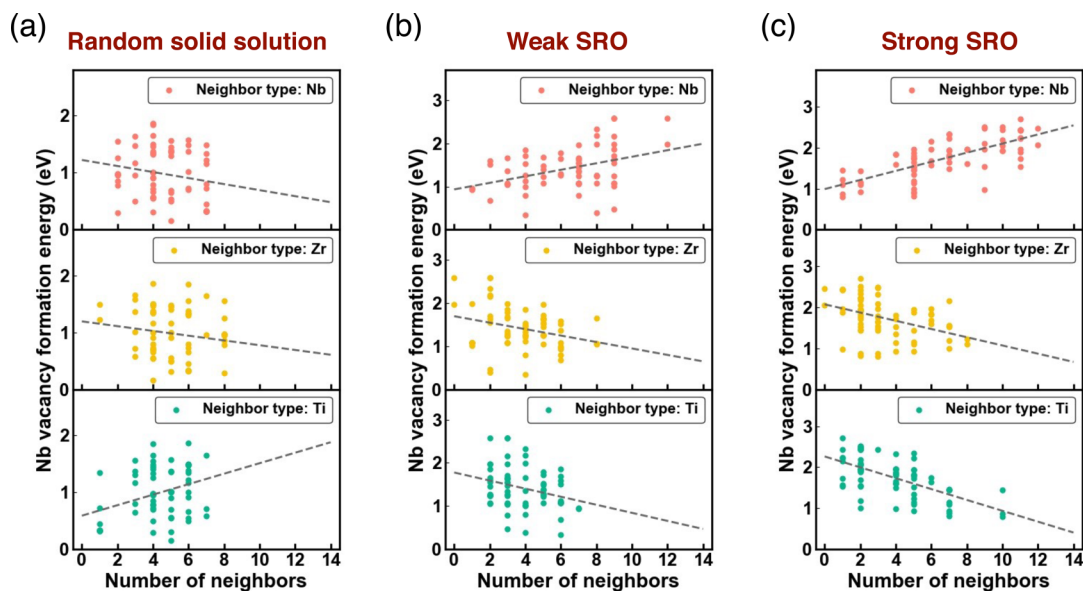
FIG. 3. Dependence of vacancy formation energy of Nb vacancy on the number of Nb, Zr, and Ti in the first and second nearest neighbors for the (a) random solid solution, (b) weak SRO, and (c) strong SRO structure.
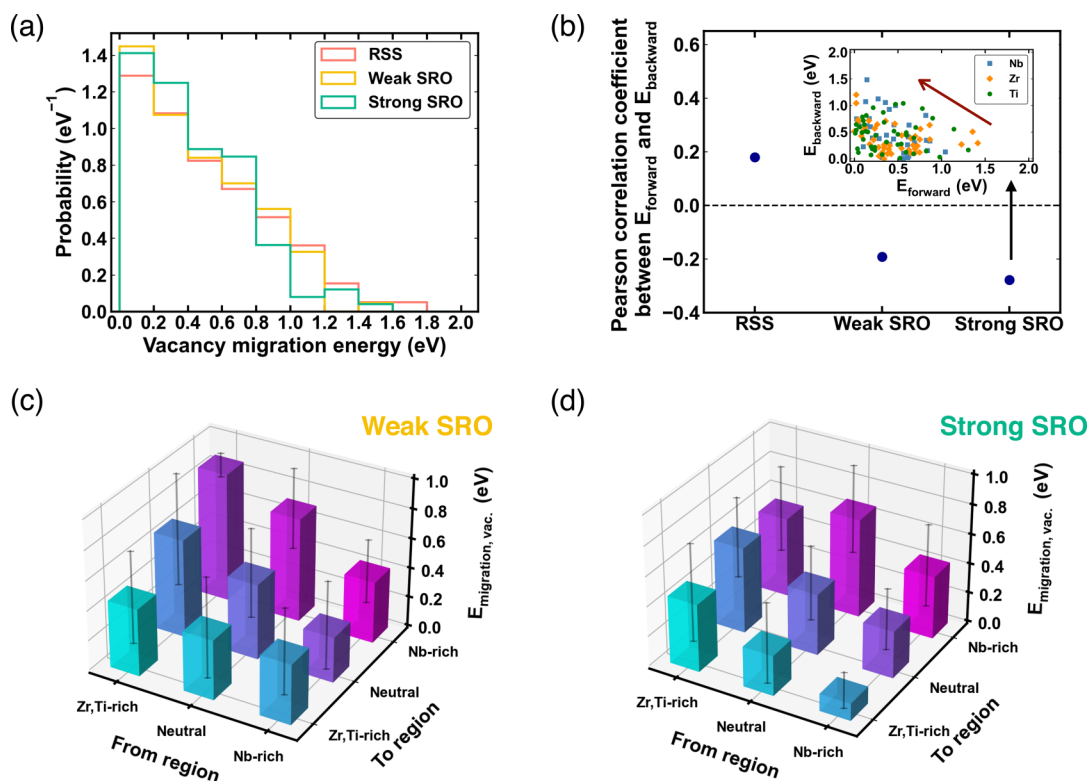

FIG. 4. (a) Distribution of vacancy migration energy. (b) Pearson correlation between the forward and backward migration energy. The inset shows the negative correlation for the strong SRO structure. (c) and (d) Vacancy migration barriers among different SRO regions for the weak and strong SRO structures, respectively.

SRO. Compared to the case of vacancy, the difference among structures of different degrees of SRO is smaller. The interstitial structures in NbZrTi can experience large structural relaxation and deviate from their initial sites and configurations. The E_f^i distributions for different final dumbbell configurations are shown in Fig. 5(b). The relative order of E_f^i is the same for RSS and SRO structures with $E_f^{Ti-Ti} < E_f^{Ti-Nb} < E_f^{Ti-Zr} \lesssim E_f^{other\ types}$. The Ti–Ti dumbbell has the lowest formation energy and is, therefore, more likely to form. The E_f^i tends to increase with the extent of SRO for Ti–Ti and Ti–Nb dumbbell, similar to the trend in E_f^v. In comparison, the change of Ti–Zr and other dumbbell types is statistically insignificant. This shows that a higher extent of SRO can effectively increase the formation energy at low-energy sites. In weak and strong SRO structures, the magnitude of E_f^i also depends on the SRO region, where E_f^i is highest in the Nb-rich region and lowest in the Zr,Ti-rich region [see Fig. 5(c)]. This is also consistent with the trend of vacancy formation energy. In the RSS structure, this trend is not observed because interstitials could rarely stay in the Nb-rich region and Ti–Ti dumbbell was more frequently formed in the simulated cases, which leads to a decrease in the formation energy.

The occurrence probabilities of different dumbbell types and directions are presented in Figs. 6(a) and 6(b) for weak and strong SRO structures, respectively. The Ti-containing interstitials have a

high occurrence probability, which is consistent with their lower E_f^i. The Ti–Ti dumbbell has a strong preference for $\langle 110 \rangle$ direction. The Ti–Nb interstitial has a high probability to form either $\langle 110 \rangle$ or $\langle 111 \rangle$ dumbbell. For other atom types, $\langle 110 \rangle$ direction is also preferred, whereas the $\langle 100 \rangle$ direction is less likely to form. Unconventional interstitial directions for BCC structures, such as $\langle 112 \rangle$, $\langle 113 \rangle$, and $\langle 013 \rangle$ dumbbells, have an increased probability to form with the increase in SRO, but still occupy a low fraction compared with $\langle 111 \rangle$ or $\langle 110 \rangle$ direction. The conventional and unconventional directions have comparable formation energies and both correspond to the local minima of interstitial configurations. We note that these unconventional directions occur mostly in the Zr, Ti-rich region and their formation could be related to the preferred electron charge distribution in these local regions. In addition, the large local lattice distortion of BCC MPEA can lead to dumbbell directions that deviate from a clear $\langle 111 \rangle$ or $\langle 110 \rangle$ direction.

Figure 6(c) shows the initial and final region of interstitials before and after structural optimization. Interstitial atoms initially positioned in the high-energy region (Nb-rich region) have a high probability to find their local minima in the other SRO regions with lower energies. Interstitials from the neutral region have a tendency to be stabilized in the Zr,Ti-rich region and can rarely move to the Nb-rich region. Interstitials initially from the Zr,Ti-rich region mostly stay in
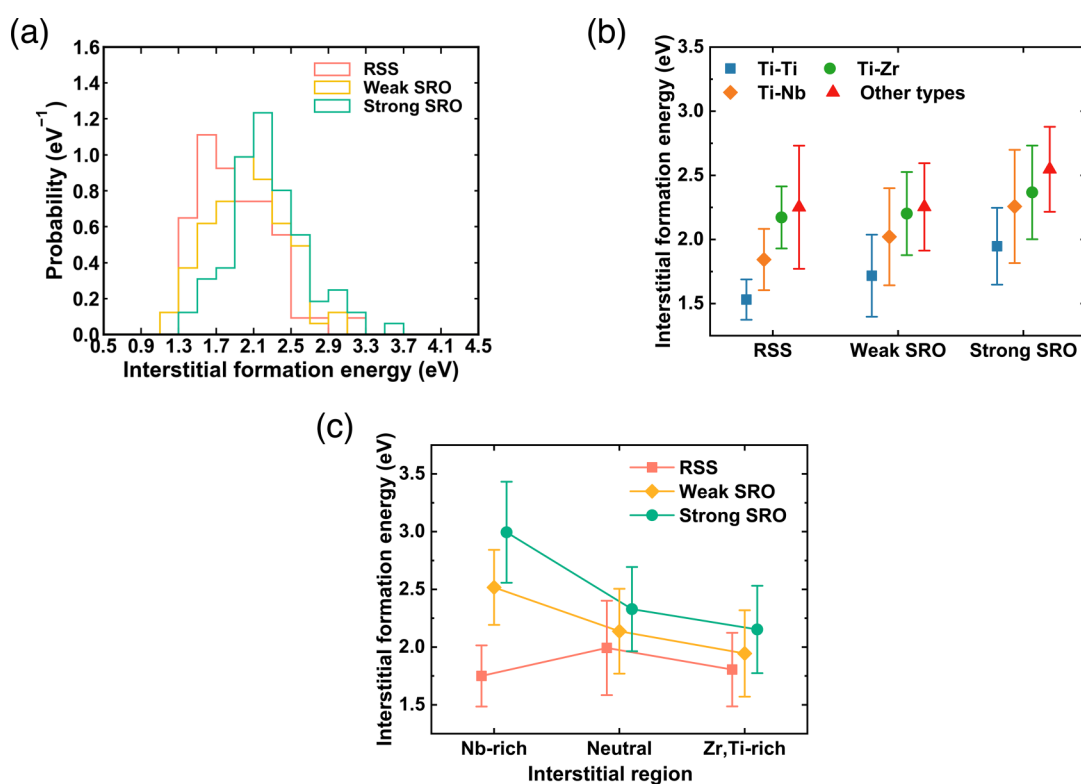

FIG. 5. (a) Distribution of interstitial formation energy for structures of different degrees of SRO. (b) Interstitial formation energy for different types of interstitial configurations (dumbbell types: Ti–Ti, Ti–Zr, Ti–Nb, and other types). All the interstitial configurations without Ti are grouped together due to their low occurrence probabilities. (c) Interstitial formation energy in different SRO regions.

the Zr,Ti-rich environment. For conventional metals, interstitials mostly have their local minima at their initial lattice sites. However, in NbZrTi, the final stable position can differ from the initial site by dumbbell rotation, anti-site exchange, and crowdion movement. Thus, the interstitials have a tendency to be stabilized in the low-energy region during structural optimization. This result is consistent with the E_f^i trend in different SRO regions shown in Fig. 5(c), reflecting the impact of SRO on the interstitial energy landscape.

The interstitial diffusion was performed at 1000 K by AIMD simulations. Based on the slope of MSD of all atoms, the tracer diffusion coefficient (D_{tracer}), defined as MSD/($c_d \cdot 6t$) (c_d: concentration of interstitial defect in the simulated structure), is progressively reduced with the increase in SRO [see Fig. 7(a)]. The diffusion trajectories show that in SRO structures, the interstitial mostly diffuses in the Zr,Ti-rich region, which leads to a lower diffusion coefficient. This is consistent with the static calculation results of lower

interstitial energy in the Zr,Ti-rich region. Based on the interstitial MSD, the defect diffusion coefficients of SRO structures (D_{defect}) are also significantly reduced compared to RSS. Although 300 ps-long simulations have been performed for each structure, the interstitial diffusion coefficients between weak and strong SRO structures are relatively close. Several observations can be made from the AIMD defect diffusion simulations. First, the tracer correlation factor, which is defined as D_{tracer}/D_{defect}, is higher in SRO structures, indicating higher efficiency of interstitial to promote mass transport relative to RSS after normalization by the defect diffusion coefficient.[30] Second, weak and strong SRO structures exhibit large differences in diffusion dynamics, as shown in Fig. 7(b). Although the most probable dumbbell type is Ti–Ti in all three structures, the second most probable dumbbell type changes from Ti–Nb in the weak SRO structure to Ti–Zr in the strong SRO structure. Ti–Nb dumbbell has a lower energy than Ti–Zr dumbbell
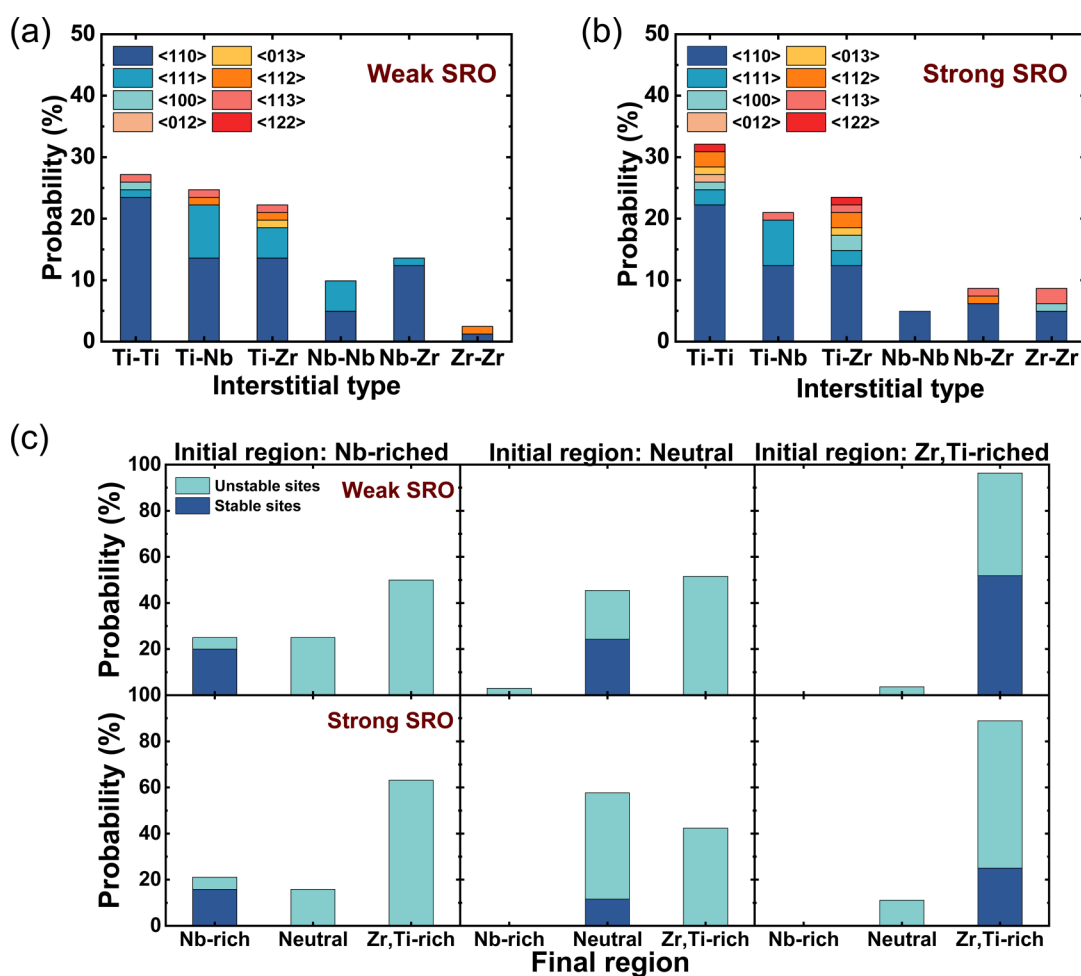

FIG. 6. (a) and (b) Occurrence probability of dumbbell interstitials of different directions in the weak and strong SRO structures. (c) Probability of interstitial movement from different initial regions to different final regions during static structural optimization. The top and bottom figures correspond to weak and strong SRO structures, respectively. Blue and green color represent interstitials that can and cannot stabilize at their initial lattice sites, respectively.

and is, therefore, energetically more favorable. However, in the strong SRO structure, stronger clustering of Ti–Zr is present in the Zr,Ti-rich region, where the interstitial is mostly confined. Such competition between the dumbbell energy state and interstitial diffusion region leads to the different migration preferences through Ti–Nb and Ti–Zr dumbbells, showing that SRO strength and tendency have a complicated effect on interstitial diffusion. Third, the limited DFT system size has an impact on the diffusion behavior. With periodic boundary condition, the modulation of alternating SRO regions cannot be guaranteed in all three dimensions. Further simulations with a larger system using classical potentials are beneficial. Figure 7(c) shows the schematics of the energy landscape for interstitial diffusion. In RSS, isolated trapping sites exist with large site-to-site energy variation. In SRO structures, localized trapping regions are present, which spatially limits the interstitial diffusion. Compared to the weak SRO structure, the extent of trapping from the Zr,Ti-rich region is more pronounced in the strong SRO structure, leading to a rougher energy landscape within the material.

IV. DISCUSSION

Based on the study of vacancy and interstitial energetics, it is shown that point defect formation energy tends to increase with the increase in SRO. For both vacancy and interstitial, Nb-rich regions and Zr,Ti-rich regions have higher and lower defect formation energies, respectively. This can lead to the migration tendency of point defects toward Zr,Ti-rich region and spatially localized diffusion in such low-energy regions. Previous classical molecular dynamics study on diffusion of small vacancy clusters in

NbZrTiV-based high-entropy alloy also showed that small vacancy clusters tend to be localized in Nb-depleted, Ti-rich regions in the SRO structure.[63] Based on this first-principles study of point defects, we expect similar SRO effects to exist in other refractory MPEAs, assuming that SRO structure is energetically favorable and can be formed within a certain range of intermediate annealing temperature in the MPEA. The SRO aggravates the difference in the local chemical environment, i.e., the elemental partition within the first several neighboring shells, leading to different energy behaviors of point defects in different SRO regions. The strong spatial inhomogeneity of the point defect energetics can result in changes of the jump rate and diffusion correlation from RSS structure to SRO structure in MPEAs. From the perspective of radiation damage, the Zr,Ti-rich SRO regions can potentially act as recombination centers to promote annihilation of point defects, reducing the agglomeration of radiation defects. In addition, the reduction of interstitial diffusion could also increase the probability of point defect recombination, as the mobilities of the fast interstitial and the slow vacancy become closer.[5] As different extents of SRO can be generated uniformly within the material by applying different annealing temperatures,[9,46] the size and the degree of SRO can be tunable with an overall effect of creating a high density of potential nanoscale point defect sinks for vacancy and interstitial annihilation. Further large-scale simulations are required to provide quantitative estimation of the enhancement of point defect recombination by SRO structures and compare their effects relative to other types of defect sinks. It is worth exploring how the degrees and dimensions of SRO or local chemical ordering could be optimized to increase the recombination probability. Besides point defects,
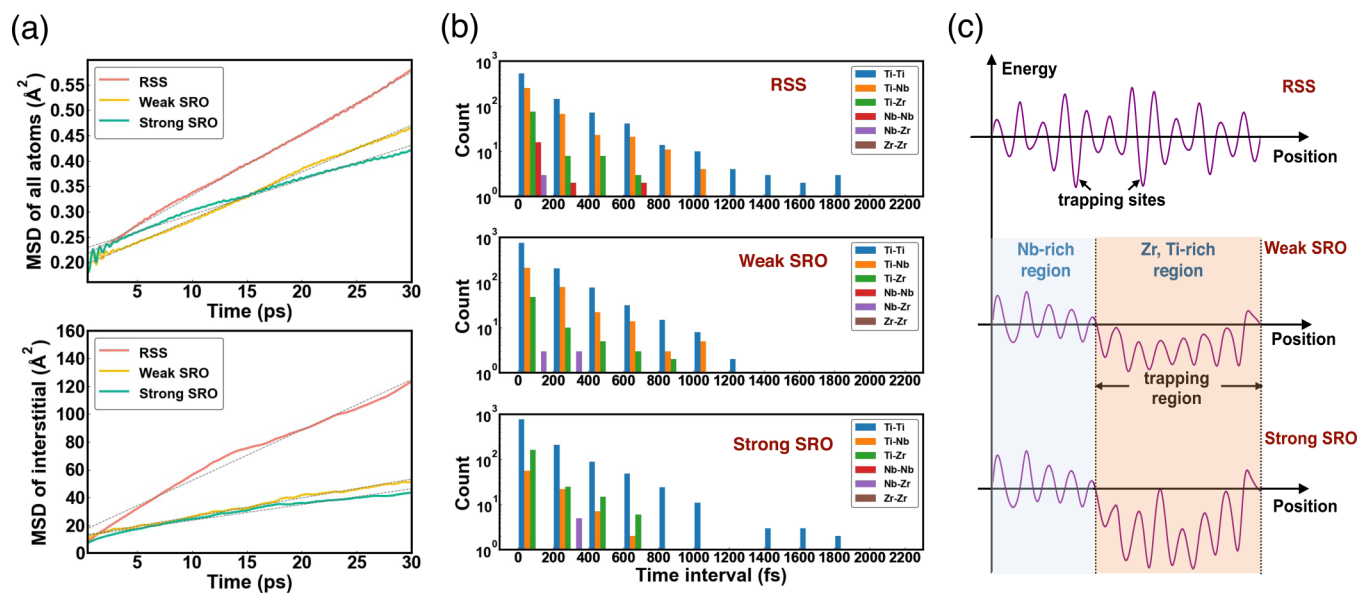
FIG. 7. (a) Mean square displacement of all atoms and the interstitial defect at 1000 K. The linear fitting to MSD is shown as a dashed line. (b) Distribution of the dwelling time at each site during the interstitial diffusion at 1000 K for the random solid solution, weak SRO structure, and strong SRO structure. (c) Schematics of the energy landscape during interstitial diffusion.

mobile defect clusters also make a large contribution to defect recombination and their diffusion behavior in SRO structures is also of great interest.[30,64]

The generation of radiation-induced defects is also influenced by SRO structures. The number of displaced atoms created by cascade collisions induced by incident particles is expected to decrease due to the increase in formation energies of point defects, assuming that the recombination probability is not greatly altered during the thermal spike period. The average formation energies of a Frenkel pair in the RSS and strong SRO structure are 2.96 $\pm$ 0.59 eV and 3.78 $\pm$ 0.64 eV, respectively. This corresponds to a difference of 28% in energy cost, which is not small considering the same elemental composition with only difference in short-range ordering tendency. For comparison, the number of surviving Frenkel pairs in Ni and NiCoFeCr after displacement cascade differs by ~29%–36%, which was attributed to the slower energy dissipation and enhanced recombination probability of NiCoFeCr.[24] Thus, from this regard, the difference in formation energy between RSS and SRO structure cannot be ignored and needs to be taken into account in the analysis of radiation defect generation. In addition, the equilibrium vacancy/interstitial concentration and defect diffusion dynamics also vary with the degree of SRO.[21,65] The SRO-dependent point defect energetics is further convoluted by the SRO evolution during the radiation period. The SRO can be destroyed by cascade collisions, leading to a more disordered state after quenching of the thermal spike region. At the same time, SRO formation or reconstruction can also be promoted by radiation-enhanced diffusion mechanism due to the high concentration of radiation-induced defects.[66] Therefore, the degree of SRO is also dose- or time-dependent during the irradiation period at high temperature, showing the necessity of understanding the impact of SRO on defect behavior in MPEAs.

V. CONCLUSION

In summary, static DFT calculations and AIMD simulations were performed to study the formation and migration of intrinsic point defects in NbZrTi with different degrees of SRO. With the decrease in the simulated annealing temperature, there is an increasing local clustering tendency among Nb atoms and Zr–Ti atoms. The formation energies of vacancy and interstitial increase with the degree of SRO and differ in different SRO regions. Although there is a wide distribution of point defect energetics due to the severe local lattice distortion, both vacancy and interstitial formation energies are statistically higher in regions enriched in Nb and lower in regions enriched in Zr and Ti. Based on the calculation of migration barriers, vacancies prefer to migrate away from the Nb-rich region toward the Zr,Ti-rich region. Interstitial diffusion is reduced compared to random solid solution and is also localized in the Zr,Ti-rich region. The occurrence probabilities of different types of dumbbells vary with the degree of SRO during diffusion, showing the complex effect from the change of the spatial energy landscape. As both vacancy and interstitial are more stable in Zr,Ti-rich regions, they can potentially serve as recombination centers with subnanoscale or nanoscale dimensions for annihilation of radiation-induced point defects. This work is important for understanding the radiation defect evolution in MPEAs and is instructive for potential SRO tuning strategy for the design of advanced radiation-tolerant materials.

SUPPLEMENTARY MATERIAL

See the supplementary material for the phonon dispersion analysis and the study of the dependence of vacancy formation energy on the local chemical environment.

AUTHOR DECLARATIONS

Conflict of Interest

The authors have no conflicts to disclose.

Author Contributions

Tan Shi: Conceptualization (equal); Data curation (equal); Formal analysis (equal); Methodology (equal); Validation (equal); Writing – original draft (equal); Writing – review & editing (equal). **Sixin Lyu:** Data curation (equal); Formal analysis (equal); Investigation (equal); Software (supporting); Validation (equal); Writing – original draft (equal); Writing – review & editing (equal). **Zhengxiong Su:** Conceptualization (supporting); Investigation (supporting). **Yunpeng Wang:** Data curation (supporting); Formal analysis (supporting). **Xi Qiu:** Data curation (supporting); Funding acquisition (supporting); Project administration (supporting). **Dan Sun:** Formal analysis (supporting); Investigation (supporting). **Yong Xin:** Investigation (supporting); Methodology (supporting); Project administration (supporting). **Wenjie Li:** Investigation (supporting); Methodology (supporting); Project administration (supporting). **Jiang Cao:** Methodology (equal); Writing – review & editing (supporting). **Qing Peng:** Methodology (equal); Writing – review & editing (supporting). **Yuanming Li:** Conceptualization (equal); Funding acquisition (equal); Investigation (equal); Project administration (equal); Supervision (equal); Writing – review & editing (equal). **Chenyang Lu:** Conceptualization (equal); Funding acquisition (equal); Investigation (equal); Project administration (equal); Supervision (equal); Writing – review & editing (equal).

DATA AVAILABILITY

The data that support the findings of this study are available from the corresponding author upon reasonable request.

REFERENCES

[1] E. P. George, W. Curtin, and C. C. Tasan, "High entropy alloys: A focused review of mechanical properties and deformation mechanisms," Acta Mater. **188**, 435–474 (2020).

[2] W. Li, D. Xie, D. Li, Y. Zhang, Y. Gao, and P. K. Liaw, "Mechanical behavior of high-entropy alloys," Prog. Mater. Sci. **118**, 100777 (2021).

[3] Y. Ikeda, B. Grabowski, and F. Körmann, "*Ab initio* phase stabilities and mechanical properties of multicomponent alloys: A comprehensive review for high entropy alloys and compositionally complex alloys," Mater. Charact. **147**, 464–511 (2019).

[4] Y. Zhang, Y. N. Osetsky, and W. J. Weber, "Tunable chemical disorder in concentrated alloys: Defect physics and radiation performance," Chem. Rev. **122**, 789–829 (2021).

[5] C. Lu, L. Niu, N. Chen, K. Jin, T. Yang, P. Xiu, Y. Zhang, F. Gao, H. Bei, S. Shi, M.-R. He, I. M. Robertson, W. J. Weber, and L. Wang, "Enhancing radiation tolerance by controlling defect mobility and migration pathways in multicomponent single-phase alloys," Nat. Commun. **7**, 13564 (2016).

[6] K. Jin, C. Lu, L. Wang, J. Qu, W. Weber, Y. Zhang, and H. Bei, "Effects of compositional complexity on the ion-irradiation induced swelling and hardening in Ni-containing equiatomic alloys," Scr. Mater. **119**, 65–70 (2016).

[7] T.-N. Yang, C. Lu, G. Velisa, K. Jin, P. Xiu, Y. Zhang, H. Bei, and L. Wang, "Influence of irradiation temperature on void swelling in NiCoFeCrMn and NiCoFeCrPd," Scr. Mater. **158**, 57–61 (2019).

[8] T.-N. Yang, C. Lu, G. Velisa, K. Jin, P. Xiu, M. L. Crespillo, Y. Zhang, H. Bei, and L. Wang, "Effect of alloying elements on defect evolution in Ni-20X binary alloys," Acta Mater. **151**, 159–168 (2018).

[9] X. Chen, Q. Wang, Z. Cheng, M. Zhu, H. Zhou, P. Jiang, L. Zhou, Q. Xue, F. Yuan, J. Zhu, X. Wu, and E. Ma, "Direct observation of chemical short-range order in a medium-entropy alloy," Nature **592**, 712–716 (2021).

[10] R. Zhang, S. Zhao, J. Ding, Y. Chong, T. Jia, C. Ophus, M. Asta, R. O. Ritchie, and A. M. Minor, "Short-range order and its impact on the CrCoNi medium-entropy alloy," Nature **581**, 283–287 (2020).

[11] D. Liu, Q. Wang, J. Wang, X. Chen, P. Jiang, F. Yuan, Z. Cheng, E. Ma, and X. Wu, "Chemical short-range order in $Fe_{50}Mn_{30}Co_{10}Cr_{10}$ high-entropy alloy," Mater. Today Nano **16**, 100139 (2021).

[12] E. Antillon, C. Woodward, S. Rao, B. Akdim, and T. Parthasarathy, "Chemical short range order strengthening in a model FCC high entropy alloy," Acta Mater. **190**, 29–42 (2020).

[13] K. Xun, B. Zhang, Q. Wang, Z. Zhang, J. Ding, and E. Ma, "Local chemical inhomogeneities in TiZrNb-based refractory high-entropy alloys," J. Mater. Sci. Technol. **135**, 221–230 (2023).

[14] S. Chen, Z. H. Aitken, S. Pattamatta, Z. Wu, Z. G. Yu, D. J. Srolovitz, P. K. Liaw, and Y.-W. Zhang, "Simultaneously enhancing the ultimate strength and ductility of high-entropy alloys via short-range ordering," Nat. Commun. **12**, 4953 (2021).

[15] Z. Lei, X. Liu, Y. Wu, H. Wang, S. Jiang, S. Wang, X. Hui, Y. Wu, B. Gault, P. Kontis *et al.*, "Enhanced strength and ductility in a high-entropy alloy via ordered oxygen complexes," Nature **563**, 546–550 (2018).

[16] Z. Su, J. Ding, M. Song, L. Jiang, T. Shi, Z. Li, S. Wang, F. Gao, D. Yun, C. Lu, and E. Ma, "Radiation-tolerant high-entropy alloys via interstitial-solute-induced chemical heterogeneities," Acta Materialia **245**, 118662 (2023).

[17] J. Ding, Q. Yu, M. Asta, and R. O. Ritchie, "Tunable stacking fault energies by tailoring local chemical order in CrCoNi medium-entropy alloys," Proc. Natl. Acad. Sci. U.S.A. **115**, 8919–8924 (2018).

[18] S. Wang, X. Liu, Z. Lei, D. Lin, F. Bian, C. Yang, M. Jiao, Q. Du, H. Wang, Y. Wu, S. H. Jiang, and Z. P. Lu, "Chemical short-range ordering and its strengthening effect in refractory high-entropy alloys," Phys. Rev. B **103**, 104107 (2021).

[19] Y. Osetsky, A. V. Barashev, L. K. Béland, Z. Yao, K. Ferasat, and Y. Zhang, "Tunable chemical complexity to control atomic diffusion in alloys," npj Comput. Mater. **6**, 1–8 (2020).

[20] Z. Su, J. Ding, M. Song, L. Jiang, T. Shi, Z. Li, and S. Wang, "Enhancing the radiation tolerance of high-entropy alloys via atomic-scale chemical heterogeneities," Acta Mater. **245**, 118662 (2023).

[21] Z. Su, T. Shi, H. Shen, L. Jiang, L. Wu, M. Song, Z. Li, S. Wang, and C. Lu, "Radiation-assisted chemical short-range order formation in high-entropy alloys," Scr. Mater. **212**, 114547 (2022).

[22] C. Li, X. Hu, T. Yang, N. K. Kumar, B. D. Wirth, and S. J. Zinkle, "Neutron irradiation response of a Co-free high entropy alloy," J. Nucl. Mater. **527**, 151838 (2019).

[23] H.-S. Do and B.-J. Lee, "Origin of radiation resistance in multi-principal element alloys," Sci. Rep. **8**, 16015 (2018).

[24] Y. Lin, T. Yang, L. Lang, C. Shan, H. Deng, W. Hu, and F. Gao, "Enhanced radiation tolerance of the Ni-Co-Cr-Fe high-entropy alloy as revealed from primary damage," Acta Mater. **196**, 133–143 (2020).

[25] S. Zhao, G. M. Stocks, and Y. Zhang, "Defect energetics of concentrated solid-solution alloys from *ab initio* calculations: $Ni_{0.5}Co_{0.5}$, $Ni_{0.5}Fe_{0.5}$, $Ni_{0.8}Fe_{0.2}$ and $Ni_{0.8}Cr_{0.2}$," Phys. Chem. Chem. Phys. **18**, 24043–24056 (2016).

[26] S. Zhao, "Defect properties in a VTaCrW equiatomic high entropy alloy (HEA) with the body centered cubic (BCC) structure," J. Mater. Sci. Technol. **44**, 133–139 (2020).

[27] H. Guan, S. Huang, J. Ding, F. Tian, Q. Xu, and J. Zhao, "Chemical environment and magnetic moment effects on point defect formations in CoCrNi-based concentrated solid-solution alloys," Acta Mater. **187**, 122–134 (2020).

[28] Q. Liu, S. Xia, Y. Su, J. Huang, S. Zhao, F. Luo, H. Liu, W. Ge, J. Xue, C. Wang, and Y. Wang, "Enhanced recombination suppresses the void swelling in bcc multi-component alloys," Materialia **20**, 101234 (2021).

[29] O. Deluigi, R. Pasianot, F. Valencia, A. Caro, D. Farkas, and E. Bringa, "Simulations of primary damage in a high entropy alloy: Probing enhanced radiation resistance," Acta Mater. **213**, 116951 (2021).

[30] S. Zhao, "Role of chemical disorder and local ordering on defect evolution in high-entropy alloys," Phys. Rev. Mater. **5**, 103604 (2021).

[31] B. Xing, X. Wang, W. J. Bowman, and P. Cao, "Short-range order localizing diffusion in multi-principal element alloys," Scr. Mater. **210**, 114450 (2022).

[32] O. N. Senkov, D. B. Miracle, K. J. Chaput, and J.-P. Couzinie, "Development and exploration of refractory high entropy alloys a review," J. Mater. Res. **33**, 3092–3128 (2018).

[33] C. Liu, W. Lu, W. Xia, C. Du, Z. Rao, J. P. Best, S. Brinckmann, J. Lu, B. Gault, G. Dehm *et al.*, "Massive interstitial solid solution alloys achieve near-theoretical strength," Nat. Commun. **13**, 1102 (2022).

[34] G. Was, D. Petti, S. Ukai, and S. Zinkle, "Materials for future nuclear energy systems," J. Nucl. Mater. **527**, 151837 (2019).

[35] T. Shi, P.-H. Lei, X. Yan, J. Li, Y.-D. Zhou, Y.-P. Wang, Z.-X. Su, Y.-K. Dou, X.-F. He, D. Yun, W. Yang, and C. Lu, "Current development of body-centered cubic high-entropy alloys for nuclear applications," Tungsten **3**, 197–217 (2021).

[36] D. King, S. Cheung, S. A. Humphry-Baker, C. Parkin, A. Couet, M. Cortie, G. Lumpkin, S. Middleburgh, and A. J. Knowles, "High temperature, low neutron cross-section high-entropy alloys in the Nb-Ti-V-Zr system," Acta Mater. **166**, 435–446 (2019).

[37] T. Shi, Z. Su, J. Li, C. Liu, J. Yang, X. He, D. Yun, Q. Peng, and C. Lu, "Distinct point defect behaviours in body-centered cubic medium-entropy alloy NbZrTi induced by severe lattice distortion," Acta Mater. **229**, 117806 (2022).

[38] O. El-Atwani, N. Li, M. Li, A. Devaraj, J. Baldwin, M. M. Schneider, D. Sobieraj, J. S. Wróbel, D. Nguyen-Manh, S. A. Maloy, and E. Martinez *et al.*, "Outstanding radiation resistance of tungsten-based high-entropy alloys," Sci. Adv. **5**, eaav2002 (2019).

[39] O. Senkov, S. Rao, K. Chaput, and C. Woodward, "Compositional effect on microstructure and properties of NbTiZr-based complex concentrated alloys," Acta Mater. **151**, 201–215 (2018).

[40] Y. Wu, Y. Cai, X. Chen, T. Wang, J. Si, L. Wang, Y. Wang, and X. Hui, "Phase composition and solid solution strengthening effect in TiZrNbMoV high-entropy alloys," Mater. Des. **83**, 651–660 (2015).

[41] P. E. Blöchl, "Projector augmented-wave method," Phys. Rev. B **50**, 17953 (1994).

[42]M. Ernzerhof and G. E. Scuseria, "Assessment of the Perdew–Burke–Ernzerhof exchange-correlation functional," J. Chem. Phys. **110**, 5029–5036 (1999).

[43]Z. Su, T. Shi, J. Yang, H. Shen, Z. Li, S. Wang, G. Ran, and C. Lu, "The effect of interstitial carbon atoms on defect evolution in high entropy alloys under helium irradiation," Acta Mater. **233**, 117955 (2022).

[44]A. Tamm, A. Aabloo, M. Klintenberg, M. Stocks, and A. Caro, "Atomic-scale properties of Ni-based FCC ternary, and quaternary alloys," Acta Mater. **99**, 307–312 (2015).

[45]W. K. Hastings, "Monte carlo sampling methods using Markov chains and their applications," Biometrika **57**, 97–109 (1970).

[46]S. Zhao, "Local ordering tendency in body-centered cubic (BCC) multi-principal element alloys," J. Phase Equilib. Diffus. **42**, 578–591 (2021).

[47]B. Widom, "Some topics in the theory of fluids," J. Chem. Phys. **39**, 2808–2812 (1963).

[48]G. Henkelman, B. P. Uberuaga, and H. Jónsson, "A climbing image nudged elastic band method for finding saddle points and minimum energy paths," J. Chem. Phys. **113**, 9901–9904 (2000).

[49]A. Zunger, S.-H. Wei, L. Ferreira, and J. E. Bernard, "Special quasirandom structures," Phys. Rev. Lett. **65**, 353 (1990).

[50]N. Anento, A. Serra, and Y. N. Osetsky, "Atomistic study of multimechanism diffusion by self-interstitial defects in α-Fe," Modell. Simul. Mater. Sci. Eng. **18**, 025008 (2010).

[51]W. Tang, E. Sanville, and G. Henkelman, "A grid-based Bader analysis algorithm without lattice bias," J. Phys.: Condens. Matter **21**, 084204 (2009).

[52]A. Stukowski, "Visualization and analysis of atomistic simulation data with OVITO—The open visualization tool," Modell. Simul. Mater. Sci. Eng. **18**, 015012 (2009).

[53]S. P. Ong, W. D. Richards, A. Jain, G. Hautier, M. Kocher, S. Cholia, D. Gunter, V. L. Chevrier, K. A. Persson, and G. Ceder, "Python Materials Genomics (pymatgen): A robust, open-source Python library for materials analysis," Comput. Mater. Sci. **68**, 314–319 (2013).

[54]S. Ishibashi, Y. Ikeda, F. Körmann, B. Grabowski, and J. Neugebauer, "Correlation analysis of strongly fluctuating atomic volumes, charges, and stresses in body-centered cubic refractory high-entropy alloys," Phys. Rev. Mater. **4**, 023608 (2020).

[55]Y. Ikeda, K. Gubaev, J. Neugebauer, B. Grabowski, and F. Körmann, "Chemically induced local lattice distortions versus structural phase transformations in compositionally complex alloys," npj Comput. Mater. **7**, 1–8 (2021).

[56]J. Cowley, "An approximate theory of order in alloys," Phys. Rev. **77**, 669 (1950).

[57]A. Takeuchi and A. Inoue, "Classification of bulk metallic glasses by atomic size difference, heat of mixing and period of constituent elements and its application to characterization of the main alloying element," Mater. Trans. **46**, 2817–2829 (2005).

[58]Y. Ikeda, A. Carreras, A. Seko, A. Togo, and I. Tanaka, "Mode decomposition based on crystallographic symmetry in the band-unfolding method," Phys. Rev. B **95**, 024305 (2017).

[59]F. Körmann, Y. Ikeda, B. Grabowski, and M. H. Sluiter, "Phonon broadening in high entropy alloys," npj Comput. Mater. **3**, 36 (2017).

[60]G. D. Samolyuk, Y. Osetsky, G. M. Stocks, and J. Morris, "Role of static displacements in stabilizing body centered cubic high entropy alloys," Phys. Rev. Lett. **126**, 025501 (2021).

[61]H. S. Oh, S. J. Kim, K. Odbadrakh, W. H. Ryu, K. N. Yoon, S. Mu, F. Körmann, Y. Ikeda, C. C. Tasan, D. Raabe, T. Egami, and E. S. Park, "Engineering atomic-level complexity in high-entropy and complex concentrated alloys," Nat. Commun. **10**, 2090 (2019).

[62]J. Hou, Y.-W. You, X.-S. Kong, J. Song, and C. Liu, "Accurate prediction of vacancy cluster structures and energetics in BCC transition metals," Acta Mater. **211**, 116860 (2021).

[63]T. Shi, X. Qiu, Y. Zhou, S. Lyu, J. Li, D. Sun, Q. Peng, Y. Xin, and C. Lu, "Unconventional energetics of small vacancy clusters in BCC high-entropy alloy $Nb_{0.75}ZrTiV_{0.5}$," J. Mater. Sci. Technol. **146**, 61–71 (2023).

[64]S. Golubov, B. Singh, and H. Trinkaus, "Defect accumulation in fcc and bcc metals and alloys under cascade damage conditions—Towards a generalisation of the production bias model," J. Nucl. Mater. **276**, 78–89 (2000).

[65]L. Koch, F. Granberg, T. Brink, D. Utt, K. Albe, F. Djurabekova, and K. Nordlund, "Local segregation versus irradiation effects in high-entropy alloys: Steady-state conditions in a driven system," J. Appl. Phys. **122**, 105106 (2017).

[66]G. S. Was, *Fundamentals of Radiation Materials Science: Metals and Alloys* (Springer, 2016).